



HAL
open science

Impact of the Nocturnal Low-Level Jet and Orographic Waves on Turbulent Motions and Energy Fluxes in the Lower Atmospheric Boundary Layer

Sayahnya Roy, Alexei Sentchev, François G Schmitt, Patrick Augustin, Marc Fourmentin

► **To cite this version:**

Sayahnya Roy, Alexei Sentchev, François G Schmitt, Patrick Augustin, Marc Fourmentin. Impact of the Nocturnal Low-Level Jet and Orographic Waves on Turbulent Motions and Energy Fluxes in the Lower Atmospheric Boundary Layer. *Boundary-Layer Meteorology*, 2021, 180 (3), pp.527-542. 10.1007/s10546-021-00629-x . hal-03319673

HAL Id: hal-03319673

<https://hal.science/hal-03319673>

Submitted on 12 Aug 2021

HAL is a multi-disciplinary open access archive for the deposit and dissemination of scientific research documents, whether they are published or not. The documents may come from teaching and research institutions in France or abroad, or from public or private research centers.

L'archive ouverte pluridisciplinaire **HAL**, est destinée au dépôt et à la diffusion de documents scientifiques de niveau recherche, publiés ou non, émanant des établissements d'enseignement et de recherche français ou étrangers, des laboratoires publics ou privés.

1 **Impact of the Nocturnal Low-Level Jet and Orographic Waves**
2 **on Turbulent Motions and Energy Fluxes in the Lower**
3 **Atmospheric Boundary Layer**

4 **Sayahnya Roy^{1,2} • Alexei Sentchev¹ • François G. Schmitt¹ • Patrick Augustin² • Marc**
5 **Fourmentin²**

6 Received: DD Month YEAR/ Accepted: DD Month YEAR/ Published online: DD Month YEAR
7 © Springer Science + Business Media B. V.

8 **Abstract** The nocturnal low-level jet (LLJ) and orographic (gravity) waves play an
9 important role in the generation of turbulence and pollutant dispersion and can affect the
10 energy production by wind turbines. Additionally, gravity waves have an influence on the
11 local mixing and turbulence within the surface layer and the vertical flux of mass into the
12 lower atmosphere. On 25 September 2017 during a field campaign, a persistent easterly LLJ
13 and gravity waves are observed simultaneously in a coastal area in the north of France. In
14 the present study, an attempt is to explore the variability of the wind speed, turbulent eddies,
15 and turbulence kinetic energy in the time-frequency and space domain using an ultrasonic
16 anemometer and a scanning wind lidar. The results reveal a significant enhancement of the
17 turbulence kinetic energy dissipation (by ~50%) due to gravity waves in the LLJ shear layer
18 (below the jet core) during the period of wave propagation. Large values of zonal and vertical
19 components of the shear stress ($\sim|0.4|$ and $\sim|1.5| \text{ m}^2 \text{ s}^{-2}$ respectively) are found during that
20 period. Large size eddies (~ 110 to 280 m), matching high-speed wind regime, are found to
21 propagate the momentum downward. This enhances the downward mass transport from the
22 LLJ shear layer to the roughness layer. Furthermore, these large-scale eddies are associated
23 with the crests while comparatively small-scale eddies are associated with the troughs of the
24 gravity wave.

✉ Sayahnya Roy
email. sayahnya1110@gmail.com

¹ Univ. Littoral Cote d'Opale, Univ. Lille, CNRS, UMR 8187, LOG, Laboratoire d'Océanologie et de Géosciences, F 62930 Wimereux, France.

² Univ. Littoral Côte d'Opale, EA 4493, LPCA, Laboratoire de Physico-Chimie de l'Atmosphère, 59140, Dunkerque, France.

25 **Keywords** Lidar measurements • Low-level Jet • Probability Density Function • Sonic
26 Anemometer • Turbulent eddies

27

28 **1 Introduction**

29 After sunset, strong wind acceleration at the altitude 100–200 m above ground level (a.g.l.)
30 is frequently observed. This phenomenon, known as the nocturnal low-level jet (LLJ), is
31 defined as concentrated airflow within the atmospheric boundary layer (ABL) over sea or
32 land surface (Banta et al. 2003). The maximum jet velocity is influenced by several factors
33 such as horizontal temperature gradients, orographic features, elevated turbulence level,
34 etc. (Birgitta 1998; Kallistratova et al. 2013). Moreover, LLJs can be formed by synoptic
35 cold fronts, thunderstorm gustfronts, drainage-flow fronts, and sea-breeze fronts. Bowen
36 (1996), Droegemeier and Wilhelmson (1987), and Darby et al. (2002) characterized the
37 LLJ profile after the front within a cold-air layer. Also, Whiteman et al. (1997) provided a
38 description of an LLJ generated at a cold-air front by large-scale density currents.
39 Furthermore, nocturnal LLJs are found to be generated by atmospheric pressure gradients
40 and baroclinity (Hoecker 1963; Bonner 1968; Mitchell et al. 1995; Zhong et al. 1996),
41 which has been widely studied to detect its influence in severe weather conditions
42 (Stensrud 1996). Prabha et al. (2008) showed that a high wind speed may occur not only
43 in the vicinity of the ABL top, but also in the shear layer, i.e. from 10 to 100 m a.g.l. Kaimal
44 and Finnigan (1994) noted that the maximum turbulence exchange occurs between a
45 canopy and the atmosphere, due to the coherent wind structures of the size of the canopy.
46 Further, Raupach et al. (1996) documented large-scale eddies generated by the interaction
47 of the wind with a large canopy (large surface roughness). They observed a modulation of
48 the eddies's size by turbulence, and showed that flow instabilities are governed by the wind
49 velocity shears.

50 Wind velocity fluctuations near the surface are involved in a cyclic process. In this
51 process the wind propagating slowly in the surface layer can be accelerated rapidly within
52 the outer layer (the uppermost 90% of the ABL, according to Rotach and Calanca 2015).
53 This is known as a “turbulent bursting event”. The downbursts due to the large roughness
54 heights were observed by Hunt and Durbin (1999) within the lower layer. Furthermore,

55 Smedman et al. (2004) showed that this type of phenomenon could be observed in the
56 presence of a LLJ tied to intense shear.

57 In the present study, an undulating motion generated by gravity or orographic waves
58 collocated with a LLJ has been observed in the lower ABL. Hoffmann et al. (2013) reported
59 that the source of many gravity waves is related to orographic features. It was also
60 documented in several studies (e.g., Fritts and Nastrom 1992; Eckermann and Vincent
61 1993; Plougonven and Teitelbaum 2003) that low-frequency gravity waves occurred in the
62 area surrounding jets and fronts, particularly in the upper troposphere regions. Those large-
63 scale gravity waves are known as inertia-gravity waves (Uccellini and Koch 1987; Guest
64 et al. 2000).

65 Gravity-wave motions are observed in the free atmosphere when the Brunt–Väisälä
66 period of oscillations in positively stratified air changes to the inertial period. Mountain-
67 waves are one of the specific cases. In the lower troposphere, wind blowing over small hills
68 starts oscillating vertically. The Coriolis force creates individual elliptic shape in the plane
69 of wind propagation and perhaps gives rise to low frequency, horizontal, inertia gravity
70 waves. These waves are frequently observed at mid-latitudes, especially in the lower
71 atmosphere (Vaughan and Hooper 2015). Recently, Wei et al. (2017) demonstrated that
72 events with small wind speed, large-scale motions (e.g., gravity waves, mesoscale
73 disturbances, or synoptic-scale variability) were capable of generating small- to large-scale
74 turbulent eddies.

75 Recent studies have focused on assessing ABL phenomena, such as LLJ or gravity
76 waves, individually (Teixeira 2014; Soufflet et al. 2019). Also, some studies focused on
77 the low-level gravity waves (Tepper 1950; Abdullah 1955). They revealed that low-level
78 gravity waves produce vertical motions, which are capable of forming convective storms.
79 Recently, Du and Chen (2019) studied the mesoscale impacts of wavelike disturbances of
80 double LLJs on convection initiation mechanisms. This recent research highlighted the
81 need to improve understanding of the relationship between gravity waves and high
82 frequency turbulence in the lower ABL. The gap of knowledge is related to the insufficient
83 simultaneous observations of both phenomena.

84 In the present study, we focus on assessing the turbulence characteristics (such as
85 turbulence kinetic energy and momentum fluxes) in the lower ABL, at 10 m height above

86 the ground, and their modulation by gravity waves propagating at large distance from the
87 ground. We also quantify the distribution of turbulent eddies in time–space and frequency
88 domain and identify the direction of kinetic energy transfer generated by turbulent eddies
89 toward the roughness layer (extending up to a few metres from the ground level).
90 Moreover, we assess the variability of turbulence kinetic energy (TKE) dissipation,
91 turbulence length scales, momentum fluxes, and turbulent bursting events in the presence
92 of a gravity wave collocated with a LLJ. The paper is organized as follows. In Sect. 2, we
93 present the data and the methods of analysis. Section 3 contains the discussion of our
94 results. Section 4 concludes the study and gives some implications of the observed large-
95 scale motions in the ABL on turbulence near the ground.

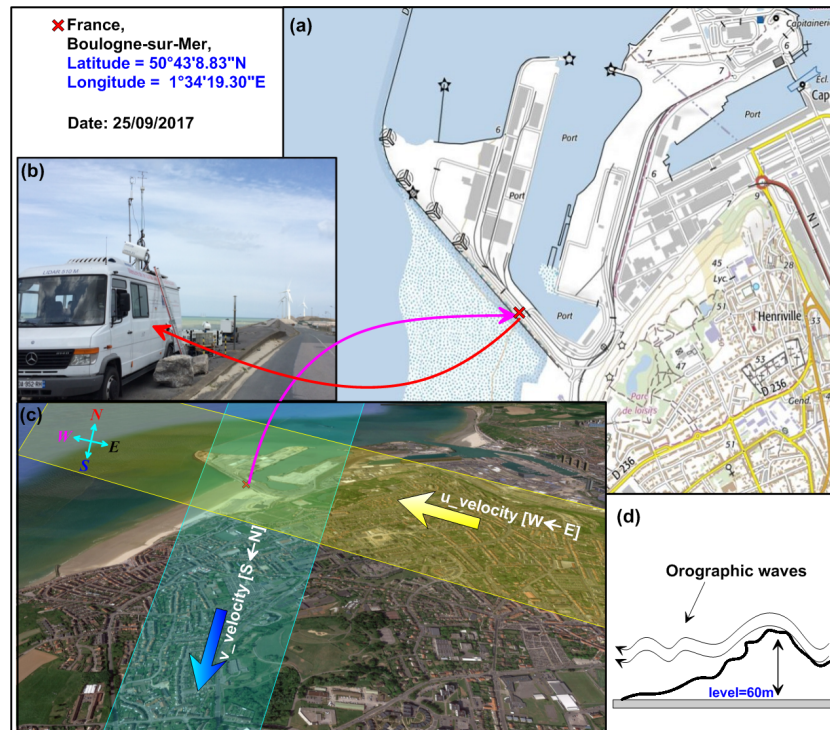
96

97 **2 Data and Methods**

98 **2.1 Study Site and Wind Measurements**

99 In the frame of the EMPATIE project (Multiscale study of turbulent atmospheric
100 phenomena and their influences on wind power), an atmospheric mobile unit (UMA) was
101 deployed on 25 September 2017 (Fig. 1), near the seashore at Boulogne-sur-Mer (France).
102 Wind profiles were measured using a scanning Doppler wind lidar (LEOSPHERE,
103 Windcube WLS 100) and a sonic anemometer (model USA-1, Metek GmbH). The pulsed
104 Doppler lidar operates at 1543 nm and uses a heterodyne technique to measure the Doppler
105 shift of laser radiation backscattered by the aerosols (Augustin et al. 2020). The wind speed
106 is estimated from the Doppler shift at different vertical levels. More technical details are
107 given by Ruchith et al. (2015) and Kumer et al. (2016). During the experiment, the lidar
108 performed, consecutively, range–height indicator (RHI) scans along the north–south and
109 east–west and Doppler beam swinging (DBS) techniques (Kumer et al. 2016). The DBS
110 technique has been used to determine the temporal evolution of horizontal wind velocity
111 profiles. The RHI scans allowed us to observe the vertical and spatial structure of the lower
112 troposphere from the ground to few kilometres with a blind zone of 100 m around the lidar.
113 Moreover, vertical profiles from RHI scans have been used to measure directly the vertical
114 wind speed. The measurement strategy was constituted of two 180° RHI scans along east–
115 west and south–north axes with 1° resolution (3 min duration per each RHI scan), and a
116 75° elevation DBS technique (1 min duration).

117 Two particular periods of lidar observations were considered: the first period, P-I, from
 118 1800 to 0000 UTC (from sunset to midnight) and the second period, P-II, from 0000 to
 119 0600 UTC (from midnight to sunrise). During P-I, a LLJ collocated with gravity waves
 120 was observed in the lower troposphere. However, both phenomena (the LLJ and gravity
 121 waves) dissipated during P-II.



122
 123 **Fig. 1** Location and period of measurements in Boulogne-sur-Mer. (a) Map of topographical levels, (b)
 124 mobile atmospheric data acquisition unit of the University of Littoral Côte d'Opale located on the seashore
 125 (red cross) equipped with a sonic anemometer and lidar (Windcube WLS 100), (c) satellite image of the study
 126 area with the indication of wind directions, (d) schematic of orographic waves due to easterly wind over
 127 elevated topography

128

129 Lidar measurements were complemented by the data from an ultrasonic anemometer
 130 operating at 10-Hz (from 1800 to 0600 UTC) and provided three components of the wind
 131 velocity and temperature variations. This sonic anemometer was deployed in the roughness
 132 layer on a 7 m mast in the blind zone of the lidar. Indeed, the lidar near-field is affected by
 133 an incomplete overlap between the laser beam and the field-of-view of a telescope
 134 corresponding to the blind zone of the lidar. No data could be recorded in this zone. The
 135 first gate was 100 m and the along-beam spatial resolution was 50 m.

136 **2.2 Methodology**

137 The velocity components u , v , and w of the wind flow (measured by ultrasonic
138 anemometer) are decomposed into a mean part and fluctuating part as

$$u = \bar{u} + u', v = \bar{v} + v', w = \bar{w} + w', \quad (1)$$

139 where u, v, w are three components of the instantaneous velocity vector, $\bar{u}, \bar{v}, \bar{w}$ are 10-min
140 averaged components and $u', v',$ and w' are the corresponding velocity fluctuations. Note
141 that the positive zonal component u represents the wind blowing from the west, the positive
142 meridional component v characterizes the wind blowing from the south, and the positive
143 vertical component w describes the wind blowing upward.

144 The time-averaged Reynolds shear stress components are defined as

$$R_{uv} = -\overline{u'v'}; R_{uw} = -\overline{u'w'}; R_{vw} = -\overline{v'w'}, \quad (2)$$

145 and the turbulence kinetic energy (TKE) can be written as

$$TKE = \frac{1}{2}(\overline{u'^2} + \overline{v'^2} + \overline{w'^2}). \quad (3)$$

146 To understand the distribution of the turbulent eddy structures in the frequency domain and
147 the maximum energy-carrying frequency of the wind velocity signal, spectral analysis was
148 performed using the FFT (fast Fourier transform) algorithm. The turbulence dissipation
149 rate (ε) is estimated from instantaneous wind measurements by sonic anemometer using
150 two different methods: the energy spectra method and the second-order structure function
151 method. The velocity spectrum, which satisfies the -5/3 slope within the inertial subrange
152 (Kolmogorov 1941), can be defined as

$$E(k) = \alpha \varepsilon^{2/3} k^{-5/3}, \quad (4)$$

153 where k is the wavenumber and α is the Kolmogorov constant ($\alpha = 0.52$). The conversion
154 of the spectrum from wavenumber to frequency domain is based on Taylor's frozen
155 turbulence hypothesis (Taylor 1935) providing

$$k = 2\pi f / \bar{U}, \quad (5)$$

156 where \bar{U} is the mean wind speed. The turbulence dissipation rate is computed using one-
157 dimensional velocity spectrum $S_u(f)$ in the inertial subrange (Champagne et al. 1977) as

$$\varepsilon = \frac{2\pi}{\bar{U}} \left(\frac{f^{5/3} S_u(f)}{\alpha} \right)^{3/2}. \quad (6)$$

158 Further, velocity increments within the inertial subrange can be conveyed as the second-
 159 order structure function (SF2) using Kolmogorov's hypothesis, and it can be
 160 interconnected to ε as

$$SF2_u(r) = \overline{[u(x+r) - u(x)]^2} = \frac{1}{\alpha} \varepsilon^{2/3} r^{2/3}, \quad (7)$$

161 where r represents the spatial separations within the inertial subrange, which can be also
 162 expressed as temporal velocity increments by applying Taylor's frozen turbulence
 163 hypothesis. Finally, ε can be calculated (similar to Bodini et al. 2018) from the second-
 164 order structure function as

$$\varepsilon = \frac{1}{\bar{u}_\tau} [\alpha SF2_u(\tau)]^{3/2}, \quad (8)$$

165 where $SF2_u(\tau)$ is the second-order structure function for velocity u with respect to
 166 temporal increments τ . The turbulent length scale (L) is computed as

$$L = \frac{TKE^{3/2}}{\varepsilon}. \quad (9)$$

167 All these quantities are used in the subsequent analysis for assessing the wind
 168 variability in the roughness layer modulated by gravity-wave interaction with the LLJ.
 169 Reynolds shear stress depicts the direction of the momentum flux affected by a LLJ
 170 collocated with gravity waves. Further, the variability of TKE and ε shows the modulation
 171 of the overall energy by large-scale motions in the ABL (LLJ and the gravity waves). Time
 172 variability in wind energy is related to eddy motions of length scale given by L . Turbulent
 173 energy propagates three-dimensionally and the dominant direction of an energy flux can
 174 be quantified by the skewness. Turbulence bursts establish variations in the momentum
 175 exchanges, demonstrated by the probability density distributions and joint distributions of
 176 velocity fluctuations. In this study, quadrant analysis is used to demonstrate the impact of
 177 gravity waves on the direction of high- and low-speed eddy propagation within the
 178 roughness layer.

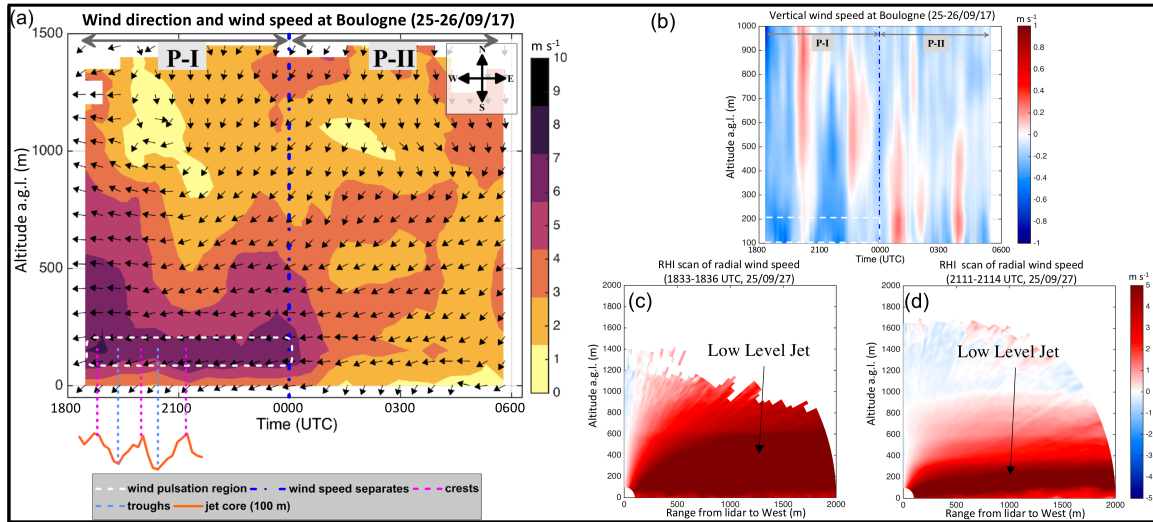
179

180 **3 Discussions of the Results**

181 **3.1 Temporal Variations of Wind**

182 The horizontal wind direction, and horizontal and vertical wind speed in the lower
 183 atmosphere observed by Doppler lidar are shown in Fig. 2a, b. In general, northerly wind
 184 is observed above the altitude 600 m from 2000 to 0600 UTC (wind speed 1 m s⁻¹ to 4 m

185 s^{-1}). However, below this altitude and above the ground, the wind direction changes to
 186 easterly for the whole period of observation. Large range of horizontal (3.5 to 8 m s^{-1}) and
 187 vertical (-0.6 to 0.3 m s^{-1}) wind speed variation are observed below 500 m during P-I.
 188 During P-II (after 0000 UTC), the wind speed decreases in the whole layer covered by
 189 observations.



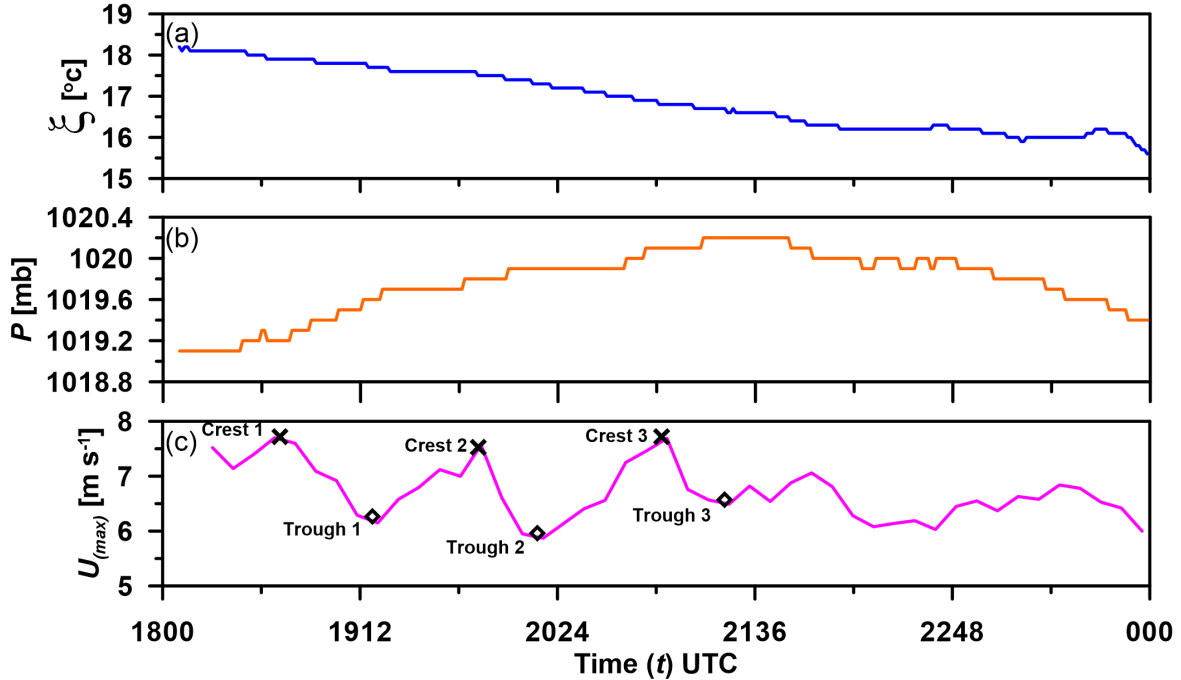
190
 191 **Fig. 2** Time–height cross-section of (a) horizontal wind direction (arrows) and speed (colour scale) and (b)
 192 vertical wind speed observed in Boulogne-sur-Mer on 25/09/17. Downward and leftward arrows represent
 193 northerly wind and easterly wind, respectively. The orange line (bottom of the figure) shows undulating
 194 patterns of maximum wind speed at 100 m . The white dashed time window corresponds to the main location
 195 of the jet core observed. RHI scan of radial wind speed toward the sea at (c) 1833 UTC and (d) 2111 UTC
 196 illustrating the LLJ phenomenon (positive values indicate flow away from lidar).

197
 198 In Fig. 2a, a blue dash-dot line separates this high-speed and low-speed wind periods in the
 199 lower troposphere ($<500\text{ m}$). During P-I and in the lower troposphere, LLJ is clearly
 200 detected by the lidar (Figs. 2c, d). The RHI scan of radial wind speed toward the sea,
 201 performed one hour after the sunset, shows a 500 m thick LLJ (Fig. 2c), which becomes
 202 thinner and decouples from the ground at about 1930 UTC (Fig. 2d). However, during the
 203 day and before the LLJ occurrence, surface wind speed was relatively low (between 2 and
 204 4 m s^{-1}) and the wind direction was mainly easterly (not shown). Although during the night,
 205 the wind speed was relatively high ($>6\text{ m s}^{-1}$), it decreased considerably from 6 m s^{-1} down
 206 to 2 m s^{-1} after the sunrise at about 530 UTC (25/09/2017). The frictional force caused by
 207 the turbulence associated with the heated ground during the day can decrease the wind

208 speed. Conversely, at the sunset (about 1730 UTC), the daytime frictional force shut down
209 (due to the collapse of convective turbulence) and consequently the air mass accelerates
210 generating the LLJ. Figure 2d represents a typical radial wind speed RHI scan obtained
211 after 1930 UTC and illustrates the shear located above and below the height of the LLJ
212 maximum wind speed (jet core), which can be an important source of turbulence,
213 particularly during the night. Observations at altitude levels ranging from 100 to 200 m
214 (white dashed rectangle in Fig. 2a, b) show the horizontal and vertical wind speed
215 variations. To investigate the nature of this variability in wind speed, we analyzed the
216 maximum wind speed at a fixed altitude of 100 m (jet core) as a function of time (Fig. 2a
217 bottom plot). Figure 2a (bottom plot) shows a sinusoidal oscillation of the wind speed. The
218 vertical wind velocity component (w) within the jet core area shows fluctuation of
219 downward motion (Fig. 2b). A quasi-harmonic oscillation of w is observed in the region
220 characterized by higher wind speed (P-I region in Fig. 2b). Later in time, during P-II, w is
221 found to be chaotic (fluctuation of upward and downward motion). Therefore the
222 variability of the horizontal wind speed components modulates the vertical wind
223 component variability.

224 To further explore the mechanisms behind the wavy nature of the atmospheric flow
225 characterized by large speed ($U_{(max)}$), the temporal evolution of the temperature (ξ),
226 pressure (P), and $U_{(max)}$ are compared in Fig. 3. Figure 3a shows an exponential decay of
227 temperature with time. The pressure (P) increases until 2136, then decreases. Wavy
228 evolution of the wind speed is clearly seen in Fig. 3c.

229



230

231 **Fig. 3** Temporal variations of (a) temperature [ξ]; (b) Pressure [P] and (c) wind speed [$U_{(max)}$] at 100 m

232

233 The study site is characterized by a complex topography with elevated topographic
 234 features (50–100 m) perpendicular to the wind. This causes gravity-wave generation and
 235 velocity undulation. Other examples given in the literature (e.g., Lott and Teitelbaum 1993;
 236 Tsuda 2014; Teixeira 2014; Sandu et al. 2019) and the present observations support the
 237 hypothesis that the wavy nature of the wind speed is due to an orographic wave of ~ 60
 238 minutes propagating from east to west. Lott and Teitelbaum (1993) stated that wave
 239 packets might be generated within the roughness layer in the temporal domain. Further,
 240 Tsuda (2014) stated that the interaction of a sheared wind flow with the topography could
 241 be a key parameter for the occurrence of orographic (gravity) waves. In the same year,
 242 Teixeira (2014) noted that downstream of the mountains, Lee wave trapping occurs. Owing
 243 to wave trapping, the formation of vortices (rotors) can be observed. Recently, Soufflet et
 244 al. (2019) showed that for small mountains, trapped Lee waves occur at a small value of
 245 the near-surface Richardson number ($Ri = N^2 / (\partial U / \partial Z)^2$), where N is the Brunt–Väisälä
 246 frequency and U is the horizontal wind speed at height Z . In our case, the value of $Ri =$
 247 0.0028 estimated, at 100 m altitude a.g.l., reveals the presence of trapped Lee waves. The
 248 small value of the inverse Froude number ($F_r^{-1} = 0.05$) also supports this condition.

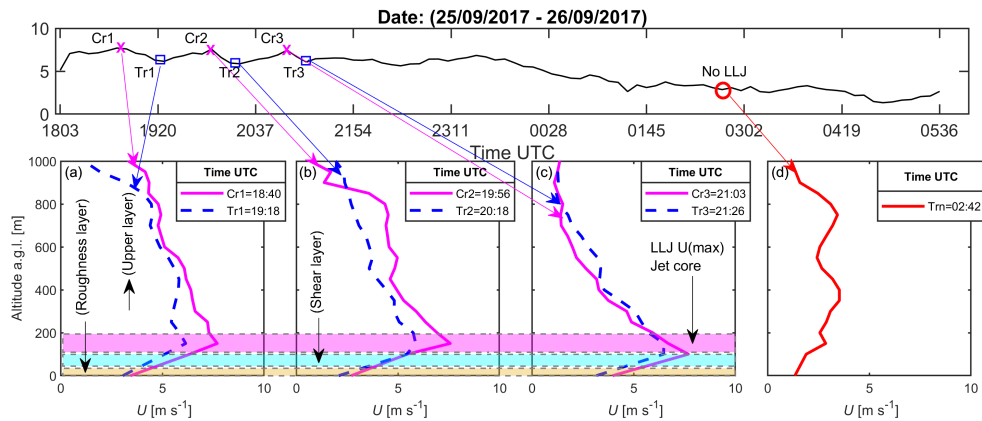
249

250 **3.2 Characteristics of Low-Level Jet**

251 The time-height section of the horizontal wind speed (Fig. 2a) and the RHI radial wind
 252 speed (Fig. 2c, d) reveal the presence of low-level jet. The observed wind profiles shown
 253 in Figure 4 are in good agreement with Stensrud (1996) and Vera et al. (2006). For a better
 254 quantification of the LLJ, we have defined four regions within the boundary layer: the
 255 roughness layer, closest to the ground, where there is a constant profile of U ; the shear
 256 layer; the LLJ jet core, and the upper layer. Three crests and troughs, referred to hereafter
 257 as Cr1-3 and Tr1-3, have been selected (Fig. 3c) for assessing the impact of LLJ and gravity
 258 waves propagation on turbulence.

259 The jet speed ($U_{max} = 8 \text{ m s}^{-1}$) is similar for these three crests (Cr1-3). As expected, the
 260 velocities are smaller ($\approx 0.75 \times U_{max}$) for the trough regions (Tr1-3). A small difference of
 261 velocities is observed in the LLJ shear layer region for trough and crest regions (Figs. 4 a–
 262 c, blue shading). Moreover, U is nearly similar for Tr1-3 compared to Cr1-3 within the
 263 roughness layer. However, the maximum differences of U (for Tr1-3 compared to Cr1-3)
 264 are observed in the upper layer and in the jet core.

265



266

267 **Fig. 4** Vertical profiles of the wind speed U corresponding to three crests and troughs of the propagating
 268 gravity wave and low wind conditions; (a) Cr1 and Tr1 (b) Cr2 and Tr2 (c) Cr3 and Tr3, and (d) low wind
 269 conditions (no Tr and Cr observed)

270

271 In this regard, Storm et al. (2019) stated that the deficiency of vertical mixing might
 272 be one of the reasons for the velocity difference in the upper layer compared to the
 273 roughness layer. These velocity differences may play an active role in accelerating the wind

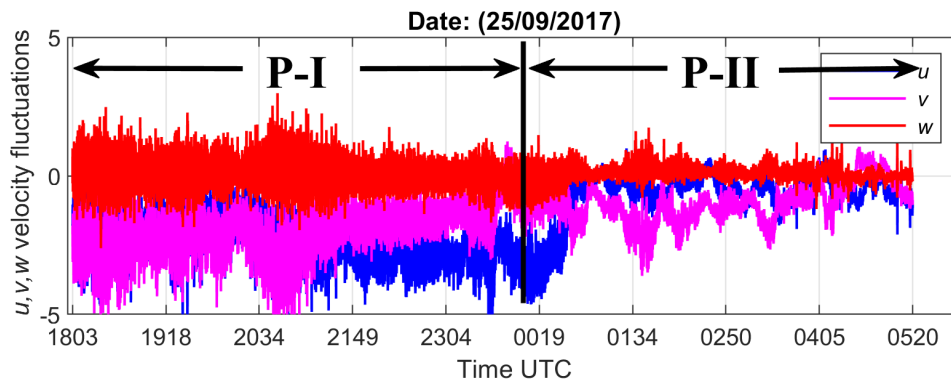
274 speed within the outer layer, unaffected by surface roughness. Furthermore, Figs. 3c and 4
 275 reveal that the gravity wave modulates the wind speed periodically.

276

277 3.3 Wind Velocity and Turbulence Assessment near the Ground

278 Since the primary focus of this study is to evaluate the turbulent properties within the
 279 roughness layer, we have analyzed the temporal variations of the velocity vector in the
 280 roughness layer using the ultrasonic anemometer data. Figure 5 shows large velocity
 281 fluctuations for u , v , w within P-I. These fluctuations are gradually reduced within P-II.
 282 This result suggests that larger levels of turbulence are generated during the gravity wave
 283 events.

284



285

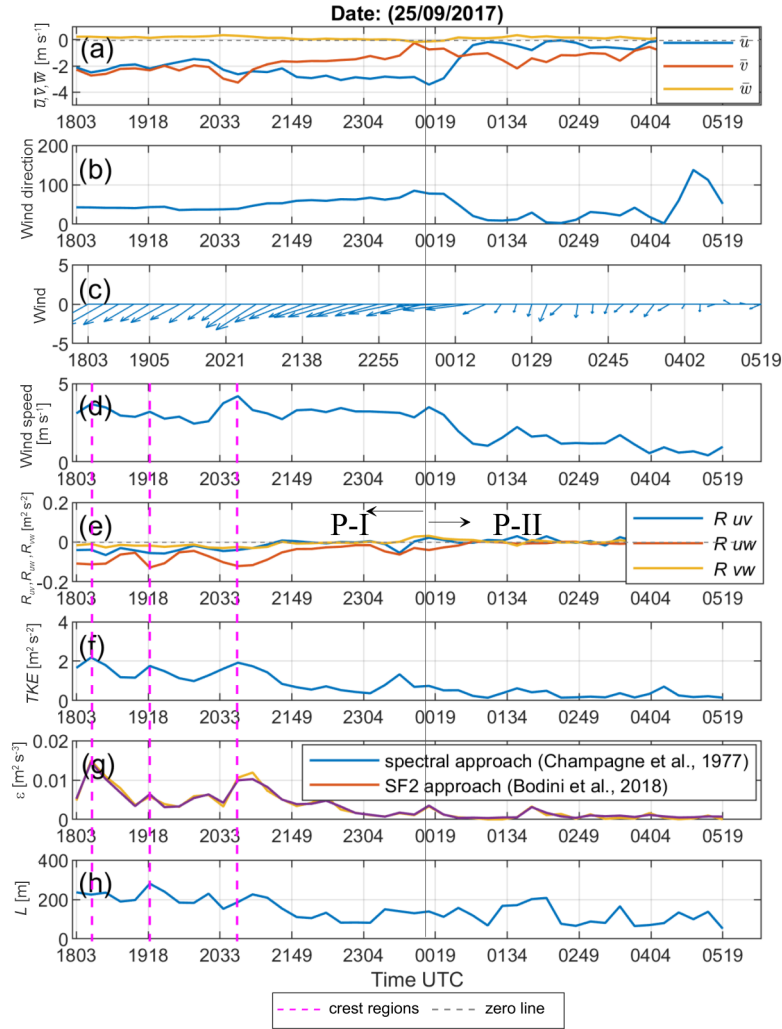
286 **Fig. 5** Time series of u , v , w wind velocity fluctuations (m s^{-1}) in the roughness layer.

287

288 Figure 6b–c shows that during the observation period, the dominant wind near the ground
 289 was from the north–east. The vertical wind component (w) is slightly positive during P-I
 290 ($w = 0.001 \text{ m s}^{-1}$) and drops to 0.000 during P-II (Fig. 6a). It is also noticed that the wind
 291 speed ranges from 3.5 to 4.5 m s^{-1} at P-I while its variation decreases from 1 to 2 m s^{-1} , at
 292 P-II (Fig. 6d). The occurrence of larger wind speed at P-I is due to the LLJ.

293 Figure 6e shows the distribution of Reynolds shear stress R_{uv} , R_{uw} , and R_{vw} as a
 294 function of time. It is evident from Fig. 6e that all three shear stress components are
 295 negative at P-I and nearly zero at P-II, which is due to a decrease in wind speed during this
 296 period. In a coordinate system aligned with the dominant wind direction, that is from east
 297 to west, negative R_{uv} values indicate momentum fluxes from north to south, negative R_{uw}
 298 values represent momentum fluxes downward, towards the roughness layer. This signifies

299 that there is a larger magnitude of momentum at P-I, and that the shear layer is a region of
 300 turbulence production. Indeed, we observed a relatively high TKE level during P-I. Figure
 301 6e also reveals that the variability of the momentum flux $\overline{u'w'}$ is similar to the maximum
 302 wind speed (U) variability shown in Fig. 3c. The gravity wave performs a modulation of
 303 the momentum flux, with larger values occurring within crests and lower values within
 304 troughs.



305
 306 **Fig. 6** Time series of (a) u , v , w wind velocity components in the roughness layer, 10-min averaged (m s^{-1});
 307 (b) wind direction with respect to the north; (c) wind velocity vector; (d) horizontal wind speed (m s^{-1}); (e)
 308 Reynolds stresses components R_{uv} , R_{uw} , and R_{vw} ($\text{m}^2 \text{s}^{-2}$); (f) Turbulence kinetic energy TKE ($\text{m}^2 \text{s}^{-2}$); (g)
 309 energy dissipation rate ε ($\text{m}^2 \text{s}^{-3}$); (h) Turbulent length scale L (m)
 310

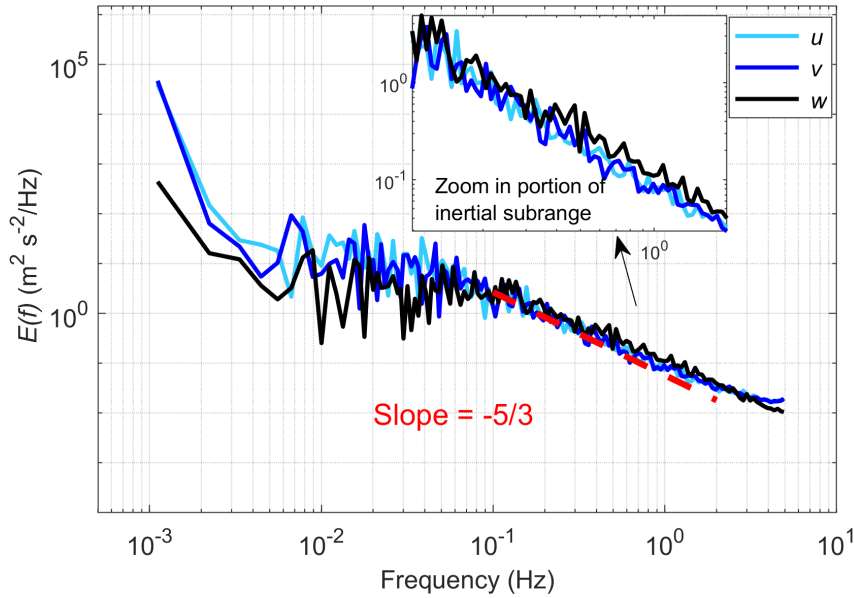
311 The temporal variation of TKE (Fig. 6f) shows a similar evolution to that of the wind
312 speed (Fig. 6d), with a variability of ~ 60 minutes during P-I. Thus, the maximum energy
313 appears concentrated at crests and minimum at troughs of the propagating gravity wave.

314 Figure 6g shows the temporal variation of ε . The wavy distribution of ε is evident
315 during P-I. This was revealed for ε estimated by two methods (spectral and SF2 approach).
316 Moreover, the LLJ associated with a gravity wave enhances the turbulent length scale L
317 P-I (Fig. 6h). Time series of L and ε (Fig. 6g–h) reveal large periodic variations during P-
318 I. Near the ground level, the magnitude of variations of the eddy dissipation and turbulent
319 length scale with respect to the mean value attains 50% and 20% respectively. These
320 variations are caused by the gravity wave propagating at the height of 100 m above the
321 ground. The values of ε deduced from zonal wind component variations by the spectral
322 method and ranging from 0.001 to 0.015 $\text{m}^2 \text{s}^{-3}$ are found to be analogous to that estimated
323 by the structure function method.

324

325 To ensure the validity of the ε estimation, the power spectral density (PSD) of u , v , and
326 w velocity components were calculated and their distribution in frequency domain is shown
327 in Fig. 7, for one particular 10-min interval of measurements by sonic anemometer. The
328 distribution shows that the turbulence is isotropic, and the inertial subrange spans from f
329 $= 0.1$ to 2 Hz (slope $-5/3$). In this subrange, there is a Richardson–Kolmogorov energy
330 cascade. The turbulent energy is generated in the frequency range $f = 1.5 \times 10^{-2}$ to ~ 0.1
331 Hz. Within the energy-containing range (<0.1 Hz), the energy production is larger for
332 horizontal components u and v than for the vertical component w within the energy-
333 containing range (<0.1 Hz). On the contrary, in the inertial subrange, the energy level of w
334 is found slightly larger (Fig. 7). Similar results are obtained for all intervals of
335 measurements at P-I, and demonstrate the dominance of large-scale horizontal and small-
336 scale vertical turbulent motions in the flow field during the observation period (P-I). The
337 direct energy transfer through energy cascading occurs in a smaller band of the inertial
338 subrange ($f = 0.1\text{Hz} - 2$ Hz) during P-I, and in a larger band ($f = 0.05\text{Hz} - 2\text{Hz}$) during P-
339 II (results not shown).

340



341

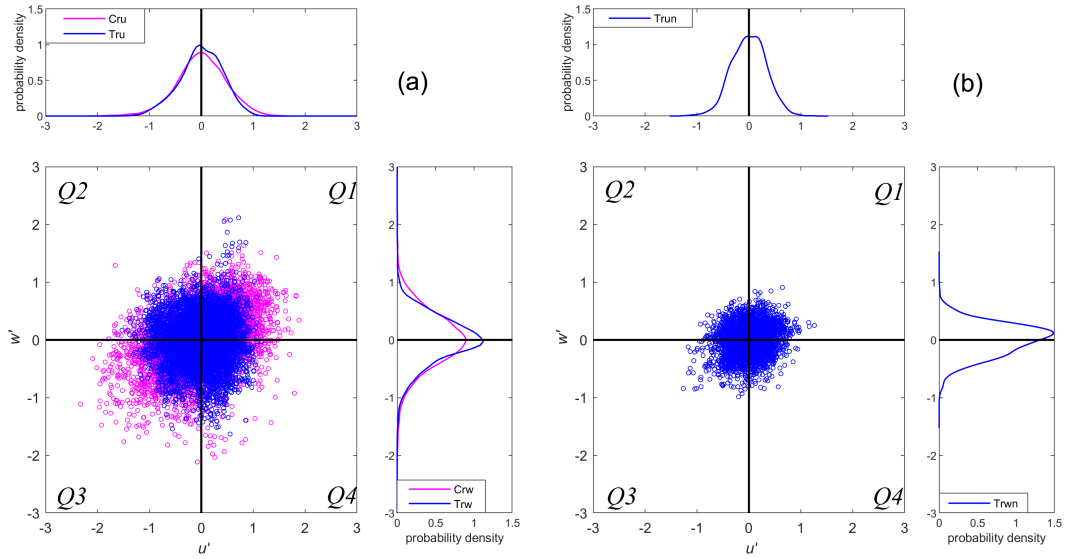
342 **Fig. 7** Power spectral density of three (u , v , w) velocity components recorded by sonic anemometer for 10
 343 min of measurement (1830–1840).

344

345 **3.4 Assessing Higher-Order Moments and Turbulent Bursting Events**

346 It was shown in Sect. 3.3 that in the roughness layer of the ABL, the shear stress R_{uw}
 347 experiences a modulation by the gravity wave. Here we analyze u' and w' time series to
 348 better understand the behaviour of their higher-order moments and probability density
 349 functions (PDFs). The PDF of u' and w' have been calculated using a method proposed in
 350 Tennekes and Lumley (1972). Figure 8 shows that the maximum of the PDF of w' is ~11%
 351 larger than that of u' , for all the troughs and crests. This means that the probability of
 352 occurrence of small fluctuations is larger for the w velocity component than for u .
 353 Furthermore, observations show that the peak values of u' and w' distributions at all the
 354 troughs are greater than that of at the crests (Fig. 8a). This suggests that the probability of
 355 the occurrence of small-scale fluctuations at troughs is larger than at crests. It may be due
 356 to the presence of small-scale eddies for lower wind speed in troughs.

357



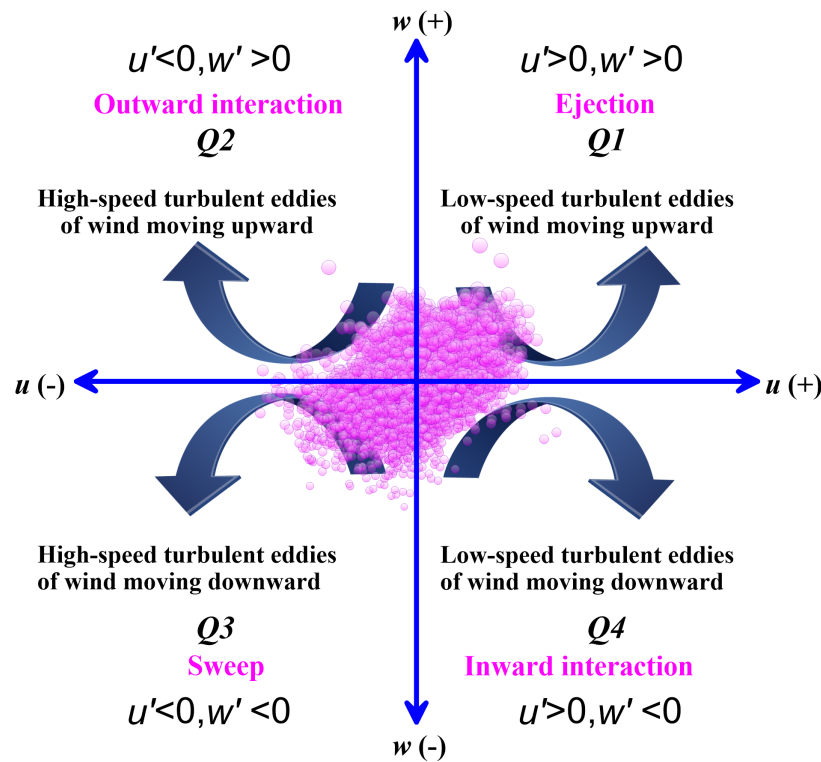
358

359 **Fig. 8** Scatter plots of u' and w' in four quadrants at the troughs (blue circles) and crests (pink circles) for P-I
 360 I (a) and P-II (b). The PDF of u' and w' are presented in the top and right side of scatter plots, respectively.
 361 The blue circles in (b) do not represent the velocity perturbations since there is no gravity wave at this time
 362

363 Comparison of panels (a) and (b) in Fig. 8 suggests that the probability of occurrences of
 364 small-scale eddies is larger at P-II, without LLJ or gravity wave phenomenon. Wind speed
 365 and shear stress are much smaller at P-II than at P-I.

366 The quadrant analysis has been frequently used to characterize the instantaneous wind
 367 speed and its direction of propagation (e.g., Lu and Willmarth 1973; Nakagawa and Nezu
 368 1977; Raupach 1981; Shaw et al. 1983). In the present study, we have used 10-min long
 369 time series at each trough and crest region during P-I and P-II. For each time frame,
 370 instantaneous u' and w' are plotted in the four quadrants. Distributions of the data (u' and
 371 w') in each quadrant represents the behaviour of turbulent bursting events (Nakagawa and
 372 Nezu 1977; Raupach 1981). Further, Raupach (1981) stated that the contribution of four
 373 events characterizes the total momentum flux ($-R_{uw}$). These events are defined in Fig. 9
 374 as (Q1) ejection event, (Q2) outward interaction, (Q3) sweep event, and (Q4) inward
 375 interaction. These events show the direction of propagation of high and low-speed turbulent
 376 eddies. In the present study, the quadrant threshold technique is used to define the
 377 influences of turbulent events in the flow field and its contribution to the total shear stress
 378 $R_{uw} = -\overline{u'w'}$ in the vertical plane (uw).

379 Figure 8a shows the distribution of the largest amount of data in $Q1$ and $Q3$ for troughs
 380 and crests during P-I. On the contrary, during P-II, an equilibrium in u' and w'
 381 distributions in all four quadrants is observed (Fig. 8b). The velocity fluctuations are more
 382 spread in $Q1$ at crests than the troughs of the gravity wave. The joint distribution of velocity
 383 fluctuations shown in Fig. 9 suggests a dominance of low-speed turbulent eddies moving
 384 upward (ejection), and high-speed turbulent eddies moving downward (sweep), during the
 385 LLJ event. However, turbulence fluctuations are homogeneous for low wind speed ≈ 0.5
 386 m s^{-1} (Fig. 8b). According to Raupach (1981) and Prabha et al. (2008), the contribution of
 387 ejection and sweep is larger than inward and outward interactions for LLJ over a large
 388 roughness. Their results are in good agreement with those presented in our study. Hunt and
 389 Durbin (1999) stated that the occurrence of intense shear shelters by the large eddies within
 390 the lower layer leads to the suppression of turbulence. The present measurements were
 391 carried out over a flat surface 10 m a.g.l. This weak motion is due to the land proximity.
 392 The dominance of low-speed upward turbulent eddies is observed in the presence of a LLJ
 393 and gravity waves, with larger undulations for crests than troughs.



394
 395 **Fig. 9** Definition diagram to portray the characteristics of u and w velocity fluctuations in the four quadrants
 396

397 **4 Conclusions**

398 Simultaneous measurements of the wind speed by a sonic anemometer and a lidar
399 performed in a coastal region of France were used for assessing flow variability and
400 turbulence in the atmospheric boundary layer. Observations revealed a dominant wind
401 from the north-east (directed from the land towards the sea) and an occurrence of a LLJ in
402 the boundary layer of the lower troposphere, during the first part of the observation period
403 (P-I), which disappeared during the second part (P-II). The wind speed was approximately
404 7 times higher during P-I, with large periodic variations observed within the roughness
405 layer during this period. We found that these periodic variations were caused by an
406 occurrence of orographic (gravity) waves generated by the wind interactions with the local
407 topography, i.e., limited height coastal relief perpendicular to the wind. To the best of our
408 knowledge, the gravity waves collocated with LLJ have been documented for the first time
409 in the coastal region of northeastern France, sought to be a flat plain with only few raised
410 orographic features.

411 Our analysis revealed a modulation of turbulence characteristics in the lower ABL (in
412 the vicinity of the ground) by the gravity waves propagating ~ 100 m above the ground.
413 The major effects of the gravity waves on local turbulence are the following:

- 414 1. The generation of a shear stress of zonal and vertical components appeared larger than
415 that of the meridional component. Larger values of the shear stress and downward
416 momentum flux were found within the crests of the propagating wave.
- 417 2. The LLJ and the associated gravity wave enhanced the wind turbulence and turbulence
418 kinetic energy dissipation near the ground.
- 419 3. Near the ground, the size of turbulent eddies varied in a wide range (from 110 m to 280
420 m) with respect to the wind speed variation controlled by the gravity wave. The size of
421 turbulent eddies was found larger within the wave's crests, while smaller size turbulent
422 eddies were associated with the troughs.
- 423 4. Large-size eddies were found to generate a downward momentum. This enhanced the
424 downward mass transport from the LLJ shear layer to the roughness layer.
- 425 5. Assessment of the momentum flux, specifically during the LLJ event, revealed the
426 dominance of low-speed turbulent eddies moving upward (ejection) and high-speed
427 turbulent eddies moving downward (sweep).

428 We expect that this study is helpful for understanding the boundary-layer dynamics,
429 turbulence, momentum and energy flux variability in the roughness sublayer in the
430 presence of orographic waves. Additionally, turbulence generated by gravity waves may
431 affect aerosol concentrations through turbulent mixing, and thus contribute to a complex
432 dynamics of the aerosols in the ABL.

433

434 **Acknowledgments** The EMPATIE project was funded by the Institut de Recherche Pluridisciplinaire en
435 Sciences de l'Environnement (IREPSE) and the Pôle de Recherche Environnement, Milieux Littoraux et
436 Marins (EMLM) of Université du Littoral Côte d'Opale.

437

438 **References**

439

- 440 Abdullah AJ (1955) The atmospheric solitary wave. *Bull Am Meteorol Soc* 36(10):511–518
- 441 Augustin P, Billet S, Crumeyrolle S, Deboudt K, Dieudonné E, Flament P, Fourmentin M, Guilbaud S,
442 Hanoune B, Landkocz Y, Méausoone C, Roy S, Schmitt FG, Sentchev A, Sokolov A (2020) Impact of
443 Sea Breeze Dynamics on Atmospheric Pollutants and Their Toxicity in Industrial and Urban Coastal
444 Environments. *Remote Sensing* 12(4):648
- 445 Banta RM, Pichugina YL, Newsom RK (2003) Relationship between low-level jet properties and turbulence
446 kinetic energy in the nocturnal stable boundary layer. *J Atmos Sci* 60(20):2549–2555
- 447 Bialkowski SE (1988) Real-time digital filters: infinite impulse response filters. *Analytical Chemistry*
448 60(6):403A–13A
- 449 Birgitta K (1998) Low level jets in a marine boundary layer during spring. *Contribution to Atmospheric*
450 *Physics* 71:359–373
- 451 Bodini N, Lundquist JK, Newsom RK (2018) Estimation of turbulence dissipation rate and its variability
452 from sonic anemometer and wind Doppler lidar during the XPIA field campaign. *Atmos Meas Tech*
453 11(7): 4291–4308
- 454 Bonner WD (1968) Climatology of the Low Level Jet. *Mon. Wea. Rev.* 96(12):833–850
- 455 Bowen BM (1996) Example of Reduced Turbulence during Thunderstorm Outflows. *J Appl Meteorol*
456 35(6):1028–1032
- 457 Champagne FH, Friche CA, LaRue JC, Wynagaard JC (1977) Flux measurements, flux estimation
458 techniques, and fine-scale turbulence measurements in the unstable surface layer over land. *J Atmos Sci*
459 34(3):515–530
- 460 Darby LS, Banta RM, Brewer WA, Neff WD, Marchbanks RD, McCarty BJ, Senff CJ, White AB, Angevine
461 WM, Williams EJ (2002) Vertical Variations in O₃ Concentrations before and after a Gust Front
462 Passage. *J Geophys Res* 107(D13):ACH–9

463 Droegeleier KK, Wilhelmson RB (1987) Numerical Simulation of Thunderstorm Outflow Dynamics
464 Part I: Outflow Sensitivity Experiments and Turbulence Dynamics. *J. Atmos. Sci.* 44(8):1180–1210
465 Du Y, Chen G (2019) Heavy rainfall associated with double low-level jets over Southern China. Part II:
466 convection initiation. *Mon Weather Rev* 147(2):543–565
467 Eckermann SD, Vincent RA (1993) VHF radar observations of gravity-wave production by cold fronts over
468 southern Australia. *J Atmos Sci* 50(6):785–806
469 Fritts DC, Nastrom GD (1992) Sources of mesoscale variability of gravity waves. Part II: Frontal, convective,
470 and jet stream excitation. *J Atmos Sci* 49(2):111–127
471 Guest FM, Reeder MJ, Marks CJ, Karoly DJ (2000) Inertia–gravity waves observed in the lower stratosphere
472 over Macquarie Island. *J Atmos Sci* 57(5):737–752
473 Hoecker WL (1963) Three Southerly Low-Level Jet Systems Delineated by the Weather Bureau Special
474 Pibal Network of 1961. *Mon Weather Rev* 91:573–582
475 Hoffmann L, Xue X, Alexander MJ (2013) A global view of stratospheric gravity wave hotspots located with
476 Atmospheric Infrared Sounder observations. *J Geophys Res Atmos* 118(2):416–434
477 Kaimal JC, Finnigan JJ (1994) Atmospheric boundary layer flows: their structure and measurement. Oxford
478 university press
479 Kallistratova MA, Kouznetsov RD, Kramar VF, Kuznetsov DD (2013) Profiles of wind speed variances
480 within nocturnal low-level jets observed with a sodar. *J Atmos Ocean Technol* 30(9):1970–1977
481 Kolmogorov AN (1991) The local structure of turbulence in incompressible viscous fluid for very large
482 Reynolds numbers. *Proceedings of the Royal Society of London. Series A: Mathematical and Physical*
483 *Sciences* 434(1890):9–13
484 Kumer VM, Reuder J, Dorninger M, Zauner R, Grubišić V (2016) Turbulent kinetic energy estimates from
485 profiling wind LiDAR measurements and their potential for wind energy applications. *Renew Energy*
486 99:898–910
487 Lott F, Teitelbaum H (1993) Linear unsteady mountain waves. *Tellus a* 45(3):201–220
488 Lu SS, Willmarth WW (1973) Measurements of the structure of the Reynolds stress in a turbulent boundary
489 layer. *J Fluid Mech* 60(3):481–511
490 Mitchell MJ, Arritt RW, Labas K (1995) A Climatology of the Warm Season Great Plains Low-Level Jet
491 Using Wind Profiler Observations. *Weather Forecast* 10(3):576–591
492 Nakagawa H, Nezu I (1977) Prediction of the contributions to the Reynolds stress from bursting events in
493 open-channel flows. *J Fluid Mech* 80(1):99–128
494 Prabha TV, Leclerc MY, Karipot A, Hollinger DY, Mursch-Radlgruber E (2008) Influence of nocturnal low-
495 level jets on eddy-covariance fluxes over a tall forest canopy. *Boundary-Layer Meteorol* 126(2):219–
496 236
497 Plougonven R, Teitelbaum H (2003) Comparison of a large-scale inertia-gravity wave as seen in the
498 ECMWF analyses and from radiosondes. *Geophys Res Lett* 30(18):1–4

499 Ruchith RD, Raj PE (2015) Features of nocturnal low level jet (NLLJ) observed over a tropical Indian station
500 using high resolution Doppler wind lidar. *Journal of Atmospheric and Solar-Terrestrial Physics* 123:113–
501 123

502 Raupach MR (1981) Conditional statistics of Reynolds stress in rough-wall and smooth-wall turbulent
503 boundary layers. *J Fluid Mech* 108:363–382

504 Raupach M, Finnigan JJ, Brunet Y (1996) Coherent eddies and turbulence in vegetation canopies: the mixing-
505 layer analogy. *Boundary-Layer Meteorol* 25:351–382

506 Rinne H (2010) Location-scale distributions—Linear estimation and probability plotting using MATLAB.
507 Justus–Liebig–Univ., Dept. of Economics and Management Science, Giessen, Germany

508 Rotach MW, Calanca P (2015) Boundary layer (atmospheric) and air pollution | Microclimate. *Encyclopedia*
509 *of atmospheric sciences* 1:258–264

510 Sandu I, van Niekerk A, Shepherd TG, Vosper SB, Zadra A, Bacmeister J, Beljaars A, Brown AR, Dörnbrack
511 A, McFarlane N, Pithan F (2019) Impacts of orography on large-scale atmospheric circulation. *npj*
512 *Climate and Atmospheric Science* 2(1):1–8

513 Shaw RH, Tavangar J, Ward DP (1983) Structure of the Reynolds stress in a canopy layer. *Journal of climate*
514 *and applied meteorology* 22(11):1922–31

515 Schmitt F, Schertzer D, Lovejoy S, Brunet Y (1994) Empirical study of multifractal phase transitions in
516 atmospheric turbulence. *Nonlin Process Geophys* 1: 95–104

517 Smedman AS, Högström U, Hunt JC (2004) Effects of shear sheltering in a stable atmospheric boundary
518 layer with strong shear. *Q J R Meteorol Soc* 130(596):31–50

519 Soufflet C, Lott F, Damiens F (2019) Trapped mountain waves with a critical level just below the surface. *Q*
520 *J R Meteorol Soc* 145:1503–1514

521 Stensrud DJ (1996) Importance of low-level jets to climate: A review. *J Clim* 9(8):1698–711

522 Storm B, Dudhia J, Basu S, Swift A, Giammanco I (2009) Evaluation of the weather research and forecasting
523 model on forecasting low - level jets: Implications for wind energy. *Wind Energy: An International*
524 *Journal for Progress and Applications in Wind Power Conversion Technology* 12(1):81–90

525 Taylor GI. *Statistical theory of turbulence. IV* (1935) Diffusion in a turbulent air stream. *Proceedings of the*
526 *Royal Society of London. Series A-Mathematical and Physical Sciences* 151(873):465–78

527 Teixeira MA (2014) The physics of orographic gravity wave drag. *Frontiers in Physics* 2(43) : 1–24

528 Tennekes H, Lumley JL, Lumley JL (1972) *A first course in turbulence*. MIT press

529 Tepper M (1950) A proposed mechanism of squall lines: The pressure jump line. *J Meteorol* 7(1):21–29

530 Tsuda T (2014) Characteristics of atmospheric gravity waves observed using the MU (Middle and Upper
531 atmosphere) radar and GPS (Global Positioning System) radio occultation. *Proceedings of the Japan*
532 *Academy, Series B.* 90(1):12–27

533 Uccellini LW, Koch SE (1987) The synoptic setting and possible energy sources for mesoscale wave
534 disturbances. *Mon Weather Rev* 115(3):721–9

535 Vaughan G, Hooper D (2015) Mesosphere–Stratosphere–Troposphere and Stratosphere–Troposphere Radars
536 and Wind Profilers. *Encyclopedia of Atmospheric Sciences Second Edition* (1): 29–437
537 Vera C, Baez J, Douglas M, Emmanuel CB, Marengo J, Meitin J, Nicolini M, Nogues-Paegle J, Paegle J,
538 Penalba O, Salio P (2006) The South American low-level jet experiment. *Bull Am Meteorol Soc*
539 87(1):63–78
540 Wei W, Zhang HS, Schmitt FG, Huang YX, Cai XH, Song Y, Huang X, Zhang H (2017) Investigation of
541 Turbulence behaviour in the stable boundary layer using arbitrary-order Hilbert spectra. *Boundary-Layer*
542 *Meteorol.* 163(2):311–26
543 Whiteman CD, Bian X, Zhong S (1997) Low-Level Jet Climatology from Enhanced Rawinsonde
544 Observations at a Site in the Southern Great Plains. *J Appl Meteorol* 36(10):1363–1376
545 Zhong S, Fast JD, Bian X (1996) A Case Study of the Great Plains Low-Level Jet Using Wind Profiler
546 Network Data and a High-Resolution Mesoscale Model. *Mon Weather Rev* 124(5):785–806
547
548
549